Observation of Spin-Splitter Torque in Collinear Antiferromagnetic RuO_2

Shutaro Karube,[1,2,*] Takahiro Tanaka,[1] Daichi Sugawara,[1] Naohiro Kadoguchi,[1] Makoto Kohda,[1,2,3,4] and Junsaku Nitta[1,2,3]
[1]Department of Materials Science, Tohoku University, Sendai 980-8579, Japan
[2]Center for Spintronics Research Network, Tohoku University, Sendai 980-8577, Japan
[3]Center for Science and Innovation in Spintronics (Core Research Cluster), Tohoku University, Sendai 980-8577, Japan
[4]Division for the Establishment of Frontier Sciences of the Organization for Advanced Studies, Tohoku University, Sendai 980-8577, Japan

(Received 6 November 2021; revised 10 February 2022; accepted 17 August 2022; published 19 September 2022)

The spin-splitter effect is theoretically predicted to generate an unconventional spin current with x- and z- spin polarization via the spin-split band in antiferromagnets. The generated torque, namely, spin-splitter torque, is effective for the manipulation of magnetization in an adjacent magnetic layer without an external magnetic field for spintronic devices such as MRAM. Here, we study the generation of torque in collinear antiferromagnetic RuO_2 with (100), (101), and (001) crystal planes. Next we find all x-, y-, and z-polarized spin currents depending on the Néel vector direction in $RuO_2(101)$. For $RuO_2(100)$ and (001), only y-polarized spin current was present, which is independent of the Néel vector. Using the z-polarized spin currents, we demonstrate field-free switching of the perpendicular magnetized ferromagnet at room temperature. The spin-splitter torque generated from RuO_2 is verified to be useful for the switching phenomenon and paves the way for a further understanding of the detailed mechanism of the spin-splitter effect and for developing antiferromagnetic spin-orbitronics.

DOI: 10.1103/PhysRevLett.129.137201

Remarkable breakthroughs in antiferromagnets (AFMs) [1,2] have been achieved in spintronics regarding exchange bias-induced field-free switching [3–5], the magnetic spin Hall effect (MSHE) [6,7], and the antiferromagnetic spin Hall effect (AFM-SHE) [8]. These intriguing phenomena have led to the establishment of antiferromagnetic spin-orbitronics to further manipulate magnetization effectively for spintronic devices because they are free from the restriction of symmetry regarding spin polarization of the generated spin current, like the conventional spin Hall effect (SHE). While the somewhat novel phenomena concerning unconventional spin-orbit torque in AFMs, such as $IrMn_3$ [7], $PtMn_3$ [9], and Mn_2Au [8] using 5d elements, still depend on spin-orbit coupling, it is difficult to uncover the mechanism generating the torque via the magnetic order. Recently, a spin-split band, through the antiferromagnetic order, was theoretically predicted to cause nontrivial torque, such as dampinglike (DL) torques of the x- and z-polarized spin currents, even without spin-orbit coupling. This is referred to as the spin-splitter effect (SSE) [10,11]. Although there is theoretical evidence for the SSE, it has not yet been demonstrated. It is worth noting that there are differences in spin current generation among conventional SHE [12–14], AFM-SHE [8], and the SSE [10,11] (or MSHE [6,7]). The spin polarization of the spin current from the SHE is strictly aligned to the y direction when we apply the electric field along the x direction. Whereas for AFM-SHE [8], the spin polarization, for example, the z-polarized component, can be defined by the Néel vector $\mathbf{n}$ and spin-orbit field $\mathbf{H_{SO}}$, due to local inversion symmetry breaking in the case of Mn_2Au, as $\boldsymbol{\sigma}_z \propto \mathbf{n} \times \mathbf{H_{SO}} \perp \mathbf{n}$. On the other hand, the polarization of the spin current generated via the SSE is parallel to the Néel vector, i.e., $\boldsymbol{\sigma}_z \| \mathbf{n}$. In this study, we focus on collinear antiferromagnetic RuO_2, which theoretically is expected to have the SSE [11], in order to reveal the actual physical mechanism.

We systematically extract the DL torques of all x-, y-, and z-polarized spin currents in $RuO_2(100)$, (101), (001). We find the anisotropic DL torque in all of the components and the DL torques of the z-polarized spin current, in particular $RuO_2(101)$ when applying the charge current along the [010] direction. Further, using the z-polarized spin current, we demonstrate field-free magnetization switching in the adjacent magnetic layer.

Ruthenium dioxide (RuO_2) has recently been found to be a collinear antiferromagnet through superexchange coupling between Ru and O ions by means of neutron and x-ray diffraction profiles, which has a rutile-type crystal structure, as shown in Fig. 1(a) (space group: $P4_2/mnm$) [15,16]. The Néel temperature was over 300 K [15]. The ruthenium oxide is electrically conductive, which originates from the spin density wave instability at the Fermi surface [15]. The measured conductivity in this study is very similar to those of metals (see Fig. S2 in the Supplemental Material [17]). Further, several notable properties regarding the Dirac nodal line (DNL) electronic topology [18], strain-induced superconductivity [19] near 1 K, and crystal Hall effect [20,21] in strong magnetic fields have been discovered recently. According to the

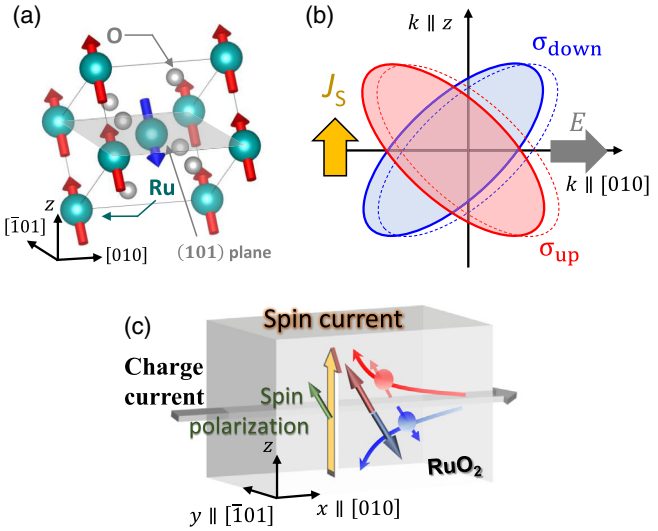

FIG. 1. (a) Crystal structure of RuO_2 with the magnetic moment aligned to [001] or [00$\bar{1}$] on the A and B sites of Ru atoms. The specific crystal plane using a gray color, corresponds to (101). (b) Spin-split band originating from the RuO_2 antiferromagnetic order at the Fermi level. When we apply an electric field E along the [010] or [0$\bar{1}$0] direction, the spin current, J_S, flowing in the z direction can be generated via the spin-splitter effect. (c) Schematic image of spin current generation in $RuO_2(101)$.

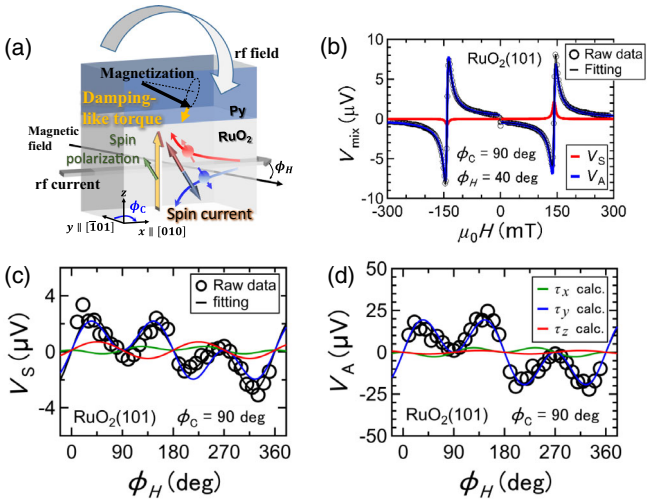

FIG. 2. (a) Schematic image of $RuO_2(101)$/Py bilayer structure during the ST-FMR measurement. In the resonance field, the magnetization uniformly oscillates owing to the rf Oersted field from the RuO_2 layer, while the spin current is generated via the SSE and injected into the Py layer. (b) ST-FMR raw data as a function of applied in-plane magnetic field. Black plots show the raw data. Black, red, and blue curves indicate fitting and calculations using the analyzed parameters. (c) Symmetric and (d) antisymmetric voltage amplitudes depending on the applied field angle for $RuO_2(101)$ when $\phi_C = 90°$. Black plots indicate the extracted values from Fig. 2(b). Black, red, blue, and green curves represent the fitting and calculations of τ_x, τ_y, and τ_z, from the analyses using Eqs. (1) and (2).

reported diffraction measurements [15,16], the Néel vector is along [001] or [00$\bar{1}$], but is not strictly aligned and somewhat canted from this direction. Regarding the magnetic order, the spin current, with the spin polarization aligned to the Néel vector, is driven using a spin-split band structure, as shown in Fig. 1(b). When we apply an electric field to a specific direction, in this case [010], spin current flows along the z direction shown in Fig. 1(c), with not only y polarization like conventional SHE, but also x and z polarization, as shown in Fig. 1(c). Here, we define the x and z axes as applied charge current and generated spin current directions in all of the experiments, respectively. This is advantageous for practical magnetization switching without the assistance of a magnetic field.

To elucidate the relationship between the Néel vector and the spin polarization of the generated spin current, we prepared 10 nm-thick $RuO_2(100)$, (101), and (001), which have an in-plane, canted, and perpendicular aligned Néel vector (see Fig. S1 in the Supplemental Material [17]). The longitudinal resistivities ρ_{xx} of the deposited $RuO_2(100)$, (101), and (001) are approximately 180, 60, and 55 $\mu\Omega$ cm, respectively (see Fig. S2 in the Supplemental Material [17]). Further, we deposited 5 nm-thick $Ni_{80}Fe_{20}$ (Py) as a spin detector, and 2 nm-thick AlO_x as a capping layer *in situ*.

Based on the films, we fabricated rf waveguide devices whose lateral dimension is 5×20 μm^2 by means of a lift-off process using photolithography and Ar ion milling. First, we employed spin-torque ferromagnetic resonance (ST-FMR) [22,23] at room temperature (RT), while applying a rf current at 2 dBm and 10 GHz, as shown in Fig. 2(a), to extract the DL torques of x-, y- and z-polarized spin currents, because this is one of the most reliable techniques for decomposing the three terms [24,25]. Figure 2(b) shows raw data of the detected ST-FMR signal $V_{\rm mix}$ as a function of the applied in-plane magnetic field in the case of $RuO_2(101)$. Here, ϕ_H in Figs. 2(a) and 2(b) corresponds to the angle between the field and the applied current direction. ϕ_C is the angle between the applied current direction and the specific crystal direction [[001], [$\bar{1}$01], and [100] or [010] for $RuO_2(100)$, (101), and (001), respectively]. The detected signal basically consists of the Lorentzian L and its derivative, $V_{\rm mix} = V_S L(H) + V_A \partial_H L(H)$ [22,23], where V_S and V_A correspond to the amplitudes of the Lorentzian and its derivative, respectively. As shown in Fig. 2(b), the fitting was successfully and decomposed into both the Lorentzian and its derivative. Based on the analysis, we summarized the amplitudes as a function of ϕ_H, as shown in Figs. 2(c) and 2(d). The DL and FL torques of x-, y- and z-polarized spin currents can be separated from the ϕ_H dependence using Eqs. (1) and (2) [24,25].

$$V_S(\phi_H) \propto \sin 2\phi_H [\tau_x^{\rm DL} \sin\phi_H + \tau_y^{\rm DL} \cos\phi_H + \tau_z^{\rm FL}], \quad (1)$$

$$V_A(\phi_H) \propto \sin 2\phi_H [\tau_x^{\rm FL} \sin\phi_H + \tau_y^{\rm FL} \cos\phi_H + \tau_z^{\rm DL}]. \quad (2)$$

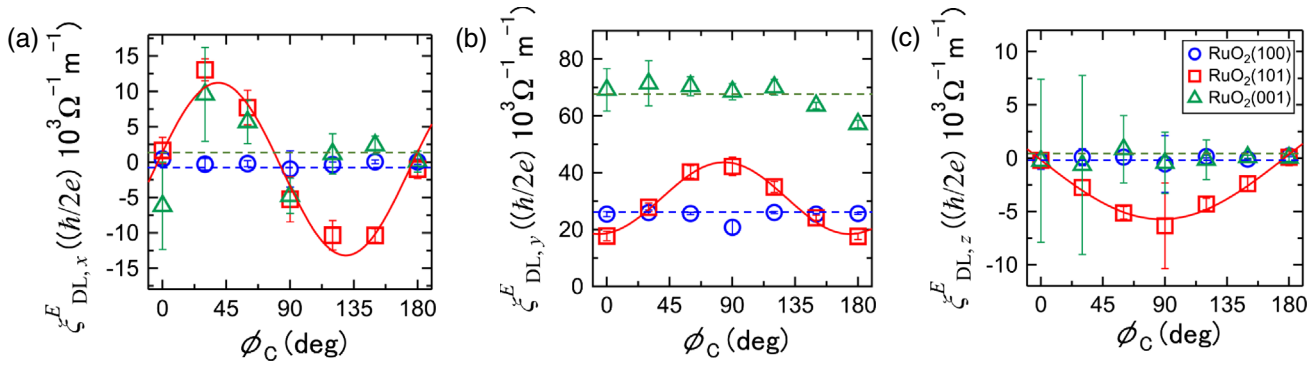

FIG. 3. DL torque efficiencies per unit electric field as a function of crystal angle ϕ_C for (a) x-, (b) y-, and (c) z-polarized spin currents. Blue open circle, red open rectangle, and green open triangle correspond to the $RuO_2(100)$, (101), and (001) cases, respectively.

Here τ_i^{DL} and τ_i^{FL} represent the amplitudes of the DL and fieldlike (FL) torque, respectively, where subscript i represents the x-, y-, and z-spin polarization components. The Oersted field generated from the RuO_2 layer makes τ_y^{FL}, which is important for the torque efficiency calculation. Through the analyses using Eqs. (1) and (2), the amplitudes were clearly fitted and decomposed into each τ_i^{DL} or τ_i^{FL}. The existence of the torques of NON y-polarized spin currents is important because this cannot be with the conventional SHE due to the strict orthogonal relationship between the applied charge current, generated spin current, and spin polarization [12–14]. Therefore, this implies that the ST-FMR signal includes both SSE and SHE.

Based on the extracted amplitudes V_S and V_A, we estimated the DL torque efficiency per unit electric field using Eqs. (3) and (4) [22].

$$\xi^E_{DL,i} = \frac{\tau_i^{DL}}{\tau_y^{FL}} \frac{e\mu_0 M_S t_{Py} t_{RuO_2}}{\hbar \rho_{xx}} \sqrt{1 + \frac{\mu_0 M_{eff}}{\mu_0 H_R}}, \tag{3}$$

$$\xi^E_{DL,z} = \frac{\tau_z^{DL}}{\tau_y^{FL}} \frac{e\mu_0 M_S t_{Py} t_{RuO_2}}{\hbar \rho_{xx}}. \tag{4}$$

Here e, $\mu_0 M_S$, t_{Py}, t_{RuO_2}, $\hbar$, ρ_{xx}, $\mu_0 M_{eff}$, and $\mu_0 H_R$ are the elementary charge, saturation magnetization of the Py layer, thickness of Py, thickness of the RuO_2 layer, the Dirac constant, longitudinal resistivity of RuO_2, effective magnetization of Py, and Py resonance field at 10 GHz, respectively. Note that $\sqrt{1 + (\mu_0 M_{eff}/\mu_0 H_R)}$ is not needed for $\xi^E_{DL,z}$ in Eq. (4) because both τ_z^{DL} and τ_y^{FL} are from the same antisymmetric voltage V_A. The effective magnetization $\mu_0 M_{eff}$ (0.8 T) was extracted from the Kittel relation in this ST-FMR measurement. The saturation magnetization of the Py layer, $\mu_0 M_S = 1.1$ T, prepared by us, was extracted from our previous report [26].

The DL torque efficiencies for each component depending on the crystal angle ϕ_C are shown in Fig. 3. These graphs show the relationship of the generated DL torque efficiency between the applied charge current and the Néel vector orientation, as defined above. Regarding $RuO_2(100)$ and (001), the DL torques of the x-, and z-polarized spin currents generated from the SSE are negligible, as shown in Figs. 3(a) and 3(c). On the other hand, a finite y component of the DL torque efficiency was found and was nearly independent of the crystal angle ϕ_C, i.e., constant. the $\xi^E_{DL,y}$ for RuO_2 (100) and (001) are $(2.5 \pm 0.2) \times 10^4$ $[(\hbar/2e)\ \Omega^{-1}\ m^{-1}]$ and $(6.7 \pm 0.5) \times 10^4$ $[(\hbar/2e)\ \Omega^{-1}\ m^{-1}]$, respectively (or 0.046 ± 0.003, 0.038 ± 0.002 for the dimensionless efficiency $\xi_{DL,y}$). Note that there is a difference in the resistivity between RuO_2 (100) and (001) (see the Supplemental Material [17]), causing a change in the amplitude relation between $\xi^E_{DL,y}$ and $\xi_{DL,y}$. Remarkably, all components of the DL torque efficiency are finite and anisotropic on the crystal angle ϕ_C in the case of $RuO_2(101)$. The DL torques of the x-, y-, and z-polarized spin currents follow Eqs. (5)–(7), respectively.

$$\xi^E_{DL,x}(\phi_C) = \xi^E_{SSE,x} \sin\phi_C \cos\phi_C, \tag{5}$$

$$\xi^E_{DL,y}(\phi_C) = \xi^E_{SHE,y} + \xi^E_{SSE,y} \sin^2\phi_C, \tag{6}$$

$$\xi^E_{DL,z}(\phi_C) = \xi^E_{SSE,z} \sin\phi_C. \tag{7}$$

Here $\xi^E_{SSE,i}(i = x, y, z)$ and $\xi^E_{SHE,y}$ are the amplitudes of the SSE and SHE for each component, respectively. We further investigated a 3 nm-thick Cu insertion case between the RuO_2 and Py layers to exclude the possibility of an exchange bias. We confirmed the same behaviors compared with the case without Cu insertion (see Figs. S3 and S4 in the Supplemental Material [17]).

The anisotropic and independent behavior regarding the crystal angle ϕ_C for all $RuO_2(100)$, (101), and (001) could be explained by the orthogonal relation between the applied charge current, spin current, and spin polarization directions, and scattering rate Γ (see Supplemental Material [17]). Next, we estimated all amplitudes for $RuO_2(101)$, as shown in Table I, based on the angular dependence. The

TABLE I. Dampinglike torque efficiencies from the spin Hall and spin-splitter effects in $RuO_2(101)$.

i	SSE, x	SSE, y	SSE, z	SHE, y
ξ_i^E $[(\hbar/2e)\ \Omega^{-1}\ \mathrm{m}^{-1}]$	$(1.2 \pm 0.1) \times 10^4$	$(2.5 \pm 0.1) \times 10^4$	$-(5.8 \pm 0.5) \times 10^3$	$(1.8 \pm 0.8) \times 10^4$
ξ_i $[-]$	0.0066 ± 0.0005	0.0138 ± 0.0001	-0.0032 ± 0.0003	0.0099 ± 0.0044
$\xi_i/\xi_{\mathrm{SHE},y}$ $[-]$	0.67	1.39	−0.32	⋯

amplitude ratio between the SSE and SHE is larger or comparable for all x-, y-, and z-spin polarization components. Thus, we have efficiently found finite but small DL torques of x-, y-, and z-polarized spin currents, even though the theory for the SSE predicted much higher efficiency values, approximately 30% [11]. This result is attributed to the AFM domain structure [27] canceling out the unidirectional Néel vector contribution due to comparable AFM domain size around 1 μm (in case of NiO [28] and Mn_2Au [29], as examples) to the lateral dimension of the sample. Although we have found twofold in-plane crystal symmetry in $RuO_2(101)$ (see Fig. S5 in the Supplemental Material [17]), the two peaks are broad, implying that the prepared RuO_2 is distorted. This could lead to the AFM domain structure reducing the unconventional torque originating from the SSE. Actually, reduction of the generated spin torque is reported in the antiferromagnetic IrMn system due to the AFM domain structure [30]. Further, for the amplitude comparison of the detected DL torque of the y-polarized spin current among $RuO_2(100)$, (101), and (001), we are currently unable to fully understand the relation even when we consider the contribution of the expected DNL topology [18]. When the electrons in RuO_2 travel on the (110) and $(\bar{1}10)$ planes, the Berry curvature driven by the DNL topology occurs, enhancing the DL torque efficiency of the y-polarized spin current. In this case, we should see the enhancement of the torque near the (110) and $(\bar{1}10)$ planes, dependent on the crystal angle ϕ_C. But we could not see any enhancement at all, implying that the DNL contribution is negligible in our system.

Next we demonstrated the field-free switching using the z-polarized spin current in $RuO_2(101)$ at RT. For the experiment, we prepared a $RuO_2(101)(10\ \mathrm{nm})/Ru(0.8\ \mathrm{nm})/Co(0.8\ \mathrm{nm})/Pt(2\ \mathrm{nm})$ multilayer structure, and fabricated a conventional Hall-bar structure whose lateral dimension is $10 \times 35\ \mu\mathrm{m}^2$ as shown in Fig. 4(a). The roles of the Ru and Pt layers are to break the RuO_2 crystallinity and to introduce a perpendicular magnetic anisotropy (PMA) of the Co layer through hexagonal closed-packed structure and spin-orbit coupling. Note that the 2 nm-thick Pt layer would not contribute to the switching of the Co layer (see the Supplemental Material [17]). As shown in Fig. 4(a), when we apply the charge current along the $[\bar{1}01]$ direction ($\phi_C = 0°$), without the z-polarized spin current, switching cannot fully occur even when applying large current [Fig. 4(b)]. When the current is applied along [010] direction ($\phi_C = 90°$), with the z-polarized spin current, 75% switching is observed at high current density regime [Fig. 4(c)]; therefore, z-spin polarization is necessary for field-free switching. This switching behavior originates from the multidomain structure of the Co layer caused by the exchange bias from the RuO_2 layer. This partial domain switching has been reported in several AFM/FM structures [3,31], meaning that this memristive behavior is inherent in the system with AFM. To achieve full switching, we need to enhance z polarized spin current by reducing AFM domain structure in RuO_2, as we discussed above. To ensure occurrence of the z polarized spin current, we confirmed an effective perpendicular field $\mu_0 H_z^{\mathrm{eff}}$ depending on the current amplitude along the [010] direction (see Fig. S6 in the Supplemental Material [17]). Here note that

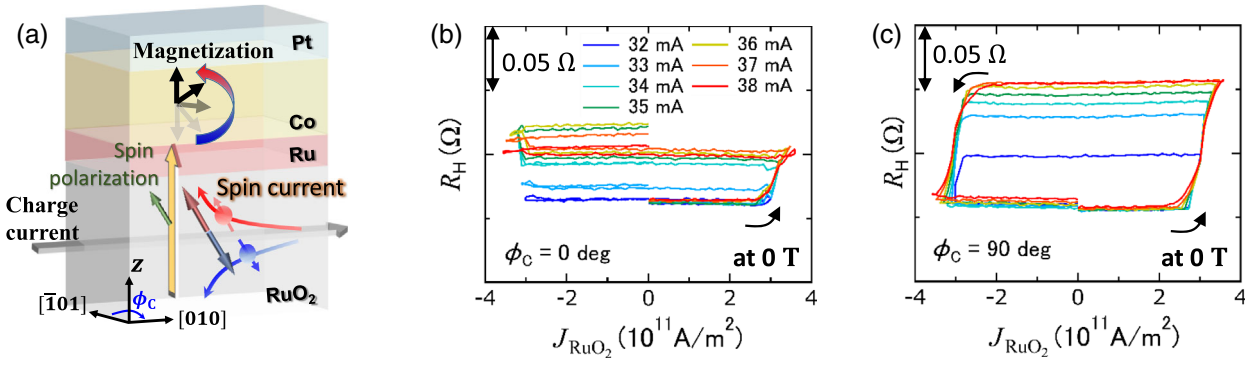

FIG. 4. (a) Schematic illustration of $RuO_2(101)(10\ \mathrm{nm})/Ru(0.8\ \mathrm{nm})/Co(0.8\ \mathrm{nm})/Pt(2.0\ \mathrm{nm})$ multilayer. The z-polarized spin current generated via the SSE is injected into the Co layer, and then the magnetization is switched without the extra external magnetic field. Hall resistance of the Co layer when applying the dc current J_{RuO_2} for the switching in the case of (b) $\phi_C = 0°$ and (c) 90°.

the FL torque of the z-polarized spin current also contributes to the switching (see Supplemental Material [17]). On the other hand, halfway switching, in the case of $\phi_C = 0°$, as shown in Fig. 4(b), would originate from the perpendicular exchange bias. We only observed the finite exchange bias when $\phi_C = 0°$, whereas it was negligible when $\phi_C = 90°$ (see the Supplemental Material [17] as shown in Fig. S8). This bias prevents reverse switching due to pinning the magnetization along the bias direction. A finite DL torque of the y-polarized spin current turns the magnetization, but is unable to fully switch it without the z-polarized spin current generated via the SSE. In the case where $\phi_C = 90°$, we observed memristive behavior with a change in the current amount. The observed memristive behavior is explained in terms of multidomain structure in the PMA Co layer induced by exchange coupling between AFM RuO_2 and ferromagnetic Co layers as is previously reported in a $PtMn/[Co/Ni]_n$ structure [3]. We emphasize that the demonstration of the field-free switching does not originate from the exchange bias, but the z-polarized spin current generated from $RuO_2(101)$. The in-plane exchange bias is induced along the $[\bar{1}01]$ direction ($\phi_C = 0°$) due to the canted Néel vector. Hereby, we have successfully demonstrated the generation of spin-splitter torque, including the DL torques of all x-, y-, and z-polarized spin currents and the field-free switching driven by the unconventional torque.

In summary, we prepared collinear antiferromagnetic $RuO_2(100)$, (101), and (001) grown epitaxially, where the SSE is theoretically expected to generate the unconventional DL torque [10,11]. Using the epitaxial films, the DL torques of all x-, y-, and z-polarized spin currents in the ruthenium oxides have been systematically investigated by means of the ST-FMR technique. Interestingly, the finite unconventional DL torques of the x- and z-polarized spin currents, depending on the Néel vector direction, have been observed in $RuO_2(101)$. These components clearly originate from the SSE. Using the z-polarized spin current from RuO_2, we have demonstrated field-free switching in the FM layer with the PMA. So, this study provides a novel spin current generation and a technique to manipulate the spins effectively for antiferromagnetic spin-orbitronics.

We would like to thank Professor Akimasa Sakuma, Professor Mikihiko Oogane, Dr. Chaoliang Zhang, and Dr. Yuta Yahagi for constructive discussions. Further, this work is partially supported by the Japan Society for the Promotion of Science (JSPS) (Grants No. 15H05699, and No. 18K14111), the Center for Spintronics Research Network at Tohoku University, and the Center for Science and Innovation in Spintronics at Tohoku University.

*karube@material.tohoku.ac.jp

[1] V. Baltz, A. Manchon, M. Tsoi, T. Moriyama, T. Ono, and Y. Tserkovnyak, Rev. Mod. Phys. **90**, 015005 (2018).
[2] A. Manchon, J. Železný, I. M. Miron, T. Jungwirth, J. Sinova, A. Thiaville, K. Garello, and P. Gambardella, Rev. Mod. Phys. **91**, 035004 (2019).
[3] S. Fukami, C. Zhang, S. DuttaGupta, A. Kurenkov, and H. Ohno, Nat. Mater. **15**, 535 (2016).
[4] Y.-W. Oh, S.-H. C. Baek, Y. M. Kim, H. Y. Lee, K.-D. Lee, C.-G. Yang, E.-S. Park, K.-S. Lee, K.-W. Kim, G. Go, J.-R. Jeong, B.-C. Min, H.-W. Lee, K.-J. Lee, and B.-G. Park, Nat. Nanotechnol. **11**, 878 (2016).
[5] Y.-C. Lau, D. Betto, K. Rode, J. M. D. Coey, and P. Stamenov, Nat. Nanotechnol. **11**, 758 (2016).
[6] M. Kimata, H. Chen, K. Kondou, S. Sugimoto, P. K. Muduli, M. Ikhlas, Y. Omori, T. Tomita, A. H. MacDonald, S. Nakatsuji, and Y. Otani, Nature (London) **565**, 627 (2019).
[7] J. Holanda, H. Saglam, V. Karakas, Z. Zang, Y. Li, R. Divan, Y. Liu, O. Ozatay, V. Novosad, J. E. Pearson, and A. Hoffmann, Phys. Rev. Lett. **124**, 087204 (2020).
[8] X. Chen, S. Shi, G. Shi, X. Fan, C. Song, X. Zhou, H. Bai, L. Liao, Y. Zhou, H. Zhang, A. Li, Y. Chen, X. Han, S. Jiang, Z. Zhu, H. Wu, X. Wang, D. Xue, H. Yang, and F. Pan, Nat. Mater. **20**, 800 (2021).
[9] H. Bai, X. F. Zhou, H. W. Zhang, W. W. Kong, L. Y. Liao, X. Y. Feng, X. Z. Chen, Y. F. You, Y. J. Zhou, L. Han, W. X. Zhu, F. Pan, X. L. Fan, and C. Song, Phys. Rev. B **104**, 104401 (2021).
[10] L. D. Yuan, Z. Wang, J.-W. Luo, E. I. Rashba, and A. Zunger, Phys. Rev. B **102**, 014422 (2020).
[11] R. González-Hernández, L. Šmejkal, K. Výborný, Y. Yahagi, J. Sinova, T. Jungwirth, and J. Železný, Phys. Rev. Lett. **126**, 127701 (2021).
[12] M. I. Dyakonov and V. I. Perel, Sov. JETP Lett. **13**, 467 (1971).
[13] T. Kimura, Y. Otani, T. Sato, S. Takahashi, and S. Maekawa, Phys. Rev. Lett. **98**, 156601 (2007).
[14] E. Saitoh, M. Ueda, H. Miyajima, and G. Tatara, Appl. Phys. Lett. **88**, 182509 (2006).
[15] T. Berlijn, P. C. Snijders, O. Delaire, H.-D. Zhou, T. A. Maier, H.-B. Cao, S.-X. Chi, M. Matsuda, Y. Wang, M. R. Koehler, P. R. C. Kent, and H. H. Weitering, Phys. Rev. Lett. **118**, 077201 (2017).
[16] Z. H. Zhu, J. Strempfer, R. R. Rao, C. A. Occhialini, J. Pelliciari, Y. Choi, T. Kawaguchi, H. You, J. F. Mitchell, Y. Shao-Horn, and R. Comin, Phys. Rev. Lett. **122**, 017202 (2019).
[17] See Supplemental Material at http://link.aps.org/supplemental/10.1103/PhysRevLett.129.137201 for detailed descriptions of sample information, magnetic parameters and mechanisms to elucidate the situation of the switching experiment.
[18] V. Jovic, R. J. Koch, S. K. Panda, H. Berger, P. Bugnon, A. Magrez, K. E. Smith, S. Biermann, C. Jozwiak, A. Bostwick, E. Rotenberg, and S. Moser, Phys. Rev. B **98**, 241101(R) (2018).
[19] M. Uchida, T. Nomoto, M. Musashi, R. Arita, and M. Kawasaki, Phys. Rev. Lett. **125**, 147001 (2020).
[20] L. Šmejkal, R. González-Hernández, T. Jungwirth, and J. Sinova1, Sci. Adv. **6**, eaaz8809 (2020).
[21] Z. Feng, X. Zhou, L. Šmejkal, L. Wu, Z. Zhu, H. Guo, R. González-Hernández, X. Wang, H. Yan, P. Qin, X. Zhang,

H. Wu, H. Chen, Z. Xia, C. Jiang, M. Coey, J. Sinova, T. Jungwirth, and Z. Liu, arXiv:2002.08712.
[22] L. Liu, T. Moriyama, D. C. Ralph, and R. A. Buhrman, Phys. Rev. Lett. **106**, 036601 (2011).
[23] D. Fang, H. Kurebayashi, J. Wunderlich, K. Výborný, L. P. Zârbo, R. P. Campion, A. Casiraghi, B. L. Gallagher, T. Jungwirth, and A. J. Ferguson, Nat. Nanotechnol. **6**, 413 (2011).
[24] T. Nan *et al.*, Nat. Commun. **11**, 4671 (2020).
[25] D. MacNeill, G. M. Stiehl, M. H. D. Guimaraes, R. A. Buhrman, J. Park, and D. C. Ralph, Nat. Phys. **13**, 300 (2017).
[26] S. Karube, D. Sugawara, C. Tang, T. Tanabe, Y. Oyama, and J. Nitta, J. Magn. Magn. Mater. **516**, 167298 (2020).
[27] F. P. Chmiel, N. W. Price, R. D. Johnson, A. D. Lamirand, J. Schad, G. van der Laan, D. T. Harris, J. Irwin, M. S. Rzchowski, C.-B. Eom, and P. G. Radaelli, Nat. Mater. **17**, 581 (2018).
[28] L. Baldrati, O. Gomonay, A. Ross, M. Filianina, R. Lebrun, R. Ramos, C. Leveille, F. Fuhrmann, T. R. Forrest, F. Maccherozzi, S. Valencia, F. Kronast, E. Saitoh, J. Sinova, and M. Kläui, Phys. Rev. Lett. **123**, 177201 (2019).
[29] S. Y. Bodnar, M. Filianina, S. P. Bommanaboyena, T. Forrest, F. Maccherozzi, A. A. Sapozhnik, Y. Skourski, M. Kläui, and M. Jourdan, Phys. Rev. B **99**, 140409(R) (2019).
[30] J. Zhou, X. Wang, Y. Liu, J. Yu, H. Fu, L. Liu, S. Chen, J. Deng, W. Lin, X. Shu, H. Y. Yoong, T. Hong, M. Matsuda, P. Yang, S. Adams, B. Yan, X. Han, and J. Chen, Sci. Adv. **5**, eaau6696 (2019).
[31] S. Lequeux, J. Sampaio, V. Cros, K. Yakushiji, A. Fukushima, R. Matsumoto, H. Kubota, S. Yuasa, and J. Grollier, Sci. Rep. **6**, 31510 (2016).